Journal of Maps

ISSN: (Print) 1744-5647 (Online) Journal homepage: https://www.tandfonline.com/loi/tjom20

Geology of the Raditladi quadrangle, Mercury (H04)

Paolo Mancinelli, Francesco Minelli, Cristina Pauselli & Costanzo Federico

To cite this article: Paolo Mancinelli, Francesco Minelli, Cristina Pauselli & Costanzo Federico (2016) Geology of the Raditladi quadrangle, Mercury (H04), Journal of Maps, 12:sup1, 190-202, DOI: 10.1080/17445647.2016.1191384

To link to this article: https://doi.org/10.1080/17445647.2016.1191384

© 2016 Paolo Mancinelli

View supplementary material

Published online: 07 Jun 2016.

Submit your article to this journal

Article views: 916

View related articles

View Crossmark data

Citing articles: 8 View citing articles

Full Terms & Conditions of access and use can be found at
https://www.tandfonline.com/action/journalInformation?journalCode=tjom20

JOURNAL OF MAPS, 2016
VOL. 12, NO. S1, 190–202
http://dx.doi.org/10.1080/17445647.2016.1191384

Taylor & Francis
Taylor & Francis Group

SCIENCE

Geology of the Raditladi quadrangle, Mercury (H04)

Paolo Mancinelli, Francesco Minelli, Cristina Pauselli and Costanzo Federico

Dipartimento di Fisica e Geologia, Università degli Studi di Perugia, Perugia, Italy

ABSTRACT

In this work, we present a 1:3,000,000-scale geologic map of the Raditladi quadrangle (H04) of Mercury. The area covers nearly 7% of the entire planet and encompasses several features of interest such as the Caloris basin, the Raditladi basin, hollow clusters and volcanic features. The mapping took advantage of the data produced during MESSENGER's orbital phase. The mapped deposits include impact-related units observed at several scales from the Caloris basin to the secondary crater chains. The Smooth Plains unit covers the majority of the area, mantling the older Intercrater Plains and Bright Intercrater Plains units. Results show that the emplacement of all the main units and the Caloris impact event, representing the main geologic events in the quadrangle, were concentrated between 3.96 and 3.72 Ga. After this intense phase, the geologic framework was modified only by local events such as impact craters and hollow formation. This map is among the first products for the detailed geologic characterization of Mercury at such a scale. It will contribute as a constraint and a support for both further local investigation and mapping, and targeting of the forthcoming BepiColombo ESA/JAXA joint exploration mission to Mercury.

ARTICLE HISTORY
Received 13 January 2016
Revised 10 May 2016
Accepted 16 May 2016

KEYWORDS
Planetary geologic map; H04 Raditladi quadrangle; Mercury

1. Introduction and background

The images and topographic data produced by the MErcury Surface, Space ENvironment, GEochemistry and Ranging spacecraft (MESSENGER) mission were used to evaluate the geologic history of the region encompassed in the Raditladi quadrangle (H04) of Mercury (22.5–66°N, 90–180°E), which covers ~7% of the planet surface. The geologic map includes a large portion of the Caloris basin (32°N, 163°E), the Raditladi basin (27°N, 120°E) and large deposits of the Northern Smooth Plains (SP) in the northern part of the quadrangle. The area was not entirely observed during the Mariner 10 mission, resulting in only the margins of the quadrangle being included in the geologic mapping produced after that mission (Frigeri, Federico, Pauselli, & Coradini, 2009; Grolier & Boyce, 1984; Guest & Greeley, 1983; Schaber & McCauley, 1980). From the maps produced after the Mariner 10 mission, the main units found to cover the area were SP and Intercrater Plains (IP) in the northern region (Grolier & Boyce, 1984) and Caloris impact-related units in the eastern and southern margins (Guest & Greeley, 1983; Schaber & McCauley, 1980). The geological characterization of the regions encompassed in the H04 quadrangle using MESSENGER data, started with the characterization of the geomorphology of the Caloris basin (Fassett et al., 2009). The first global-scale geologic map based on Mercury Dual Imaging System images covering areas observed after Mariner 10 and MESSENGER's flybys highlighted a significant geologic heterogeneity of the regions in the H04 quadrangle (Denevi et al., 2009), which was confirmed also by later work (Mancinelli, Minelli, Mondini, Pauselli, & Federico, 2015).

Beyond the Caloris basin, which is among the largest impact basins in the entire solar system, the terrains encompassed in the H04 quadrangle show intriguing morphologies related to both endogenic (e.g. volcanism and tectonic activity) and external processes (e.g. impact cratering). Among the most intriguing features observed in the quadrangle, hollows (Blewett et al., 2011, 2012) and volcanic flow morphologies (Byrne et al., 2013) were found to enrich the geologic complexity of the area.[1]

The Caloris basin is among the largest impact basins of the solar system and was first imaged during the Mariner 10 mission. The topography inside the basin is irregular with the northern part being generally higher than the southern part. The smooth materials filling the basin are deformed by a multitude of radial and circumferential structures (Byrne et al., 2012).

High-resolution images, produced during the orbital phase of the MESSENGER spacecraft, allowed for a local and detailed characterization of the geology and stratigraphy of the Raditladi basin and its surroundings (Mancinelli et al., 2015). However, a

CONTACT Paolo Mancinelli pamancinelli@gmail.com Dipartimento di Fisica e Geologia, Università degli Studi di Perugia, via A. Pascoli 06123, Perugia, Italy

© 2016 Paolo Mancinelli

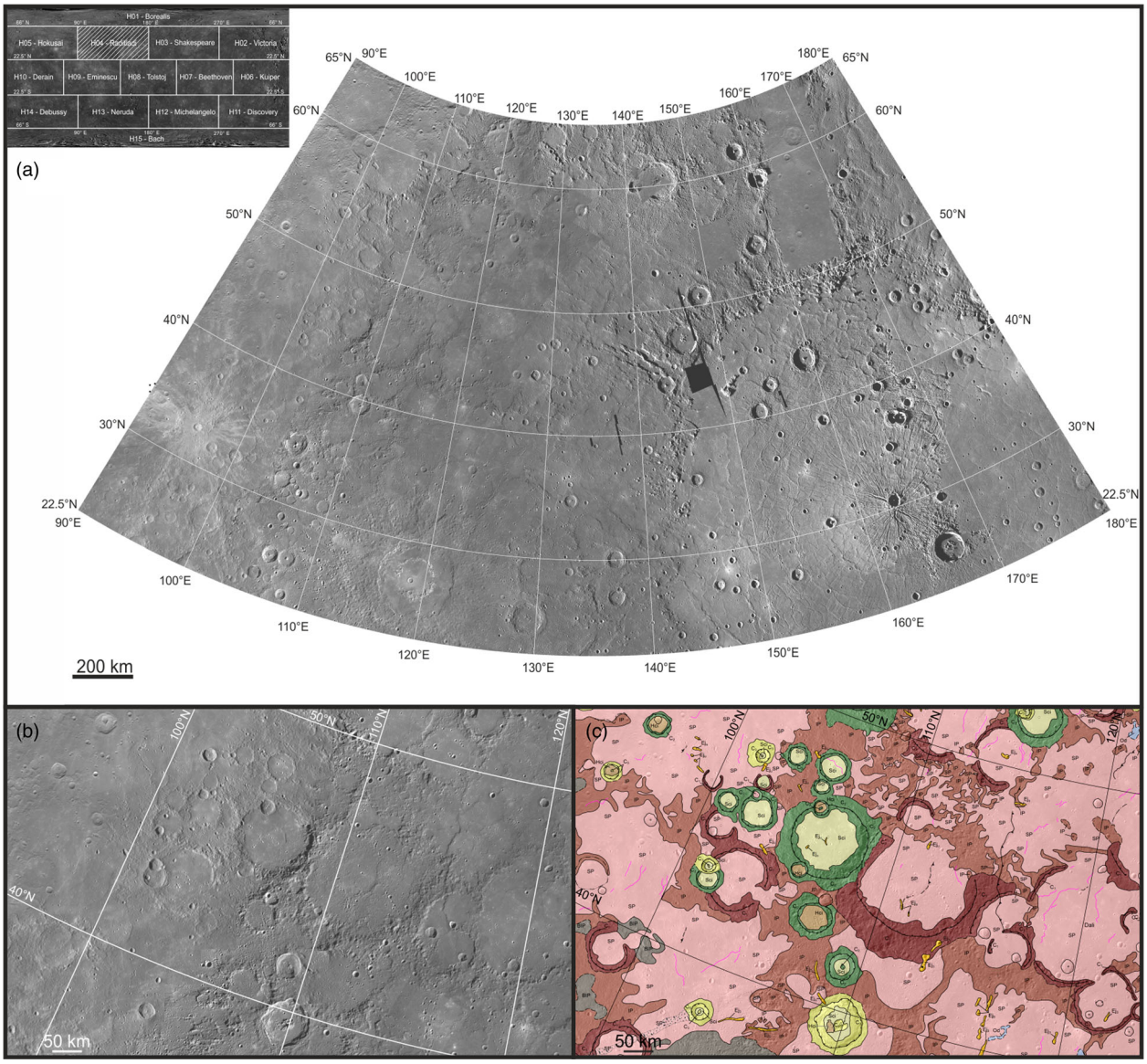

Figure 1. (a) Overview of the H04 quadrangle from the RDRBDR files mosaic. The Narrow Angle Camera (NAC) and Wide Angle Camera (WAC) images used to create these RDRBDR files were corrected to incidence angle $i = 30°$, emergence angle $e = 0°$ and phase angle $g = 30°$ with the resolution of each file composing the mosaic 256 pixels per degree – that is, ~166 m/pixel (https://pds.nasa.gov/ds-view/pds/viewDataset.jsp?dsid=MESS-H-MDIS-5-RDR-BDR-V1.0). In the small portions inside and west of Caloris where the RDRBDR data coverage was absent (44°N, 147°E), the mapping was achieved using the 250 m/pixel monochrome mosaic that is shown in the upper left inset map to locate the quadrangle. This monochrome mosaic is published on the MESSENER site (http://messenger.jhuapl.edu/the_mission/mosaics/, 20130514_complete_mono_basemap_250mpp_equirectangular.png). However, considering the different resolution between the RDRBDR and the monochrome mosaic, the RDRBDR mosaic is shown as the imagery base map on the geologic map and in all the figures of this work. Shadow zones locally found in some craters inside Caloris have not been mapped. (b) Sample area observed from the mosaic. (c) Sample area after mapping, see the text for unit descriptions. Given the latitude range in which the mapped area is found, we adopted a Lambert Conformal Conic projection with standard parallel 1 and 2 of 30° and 58° respectively, central meridian 135°, false easting and false northing of 0°, both for map and figures. The datum used in this work is the same as that used by the MESSENGER team; it approximates Mercury to a sphere of 2440.0 km of radius. This datum was used both to mosaic and to georeference the imagery base map. Scale values refer to the standard parallels.

high-resolution geologic mapping of the entire quadrangle was never produced.

2. Data

The map was built using an imagery mosaic composed of four Map Projected Basemap Reduced Data Record (RDRBDR) images produced by the MESSENGER team using images acquired during the spacecraft's orbital phase (Figure 1(a)).

To cover the entire quadrangle, three distinct topographic datasets were used to constrain the mapping and evaluate stratigraphic relationships between terrains (Figure 2).

3. Methods

We used ISIS3 software (see Software section) to create the mosaic from the original four RDRBDR

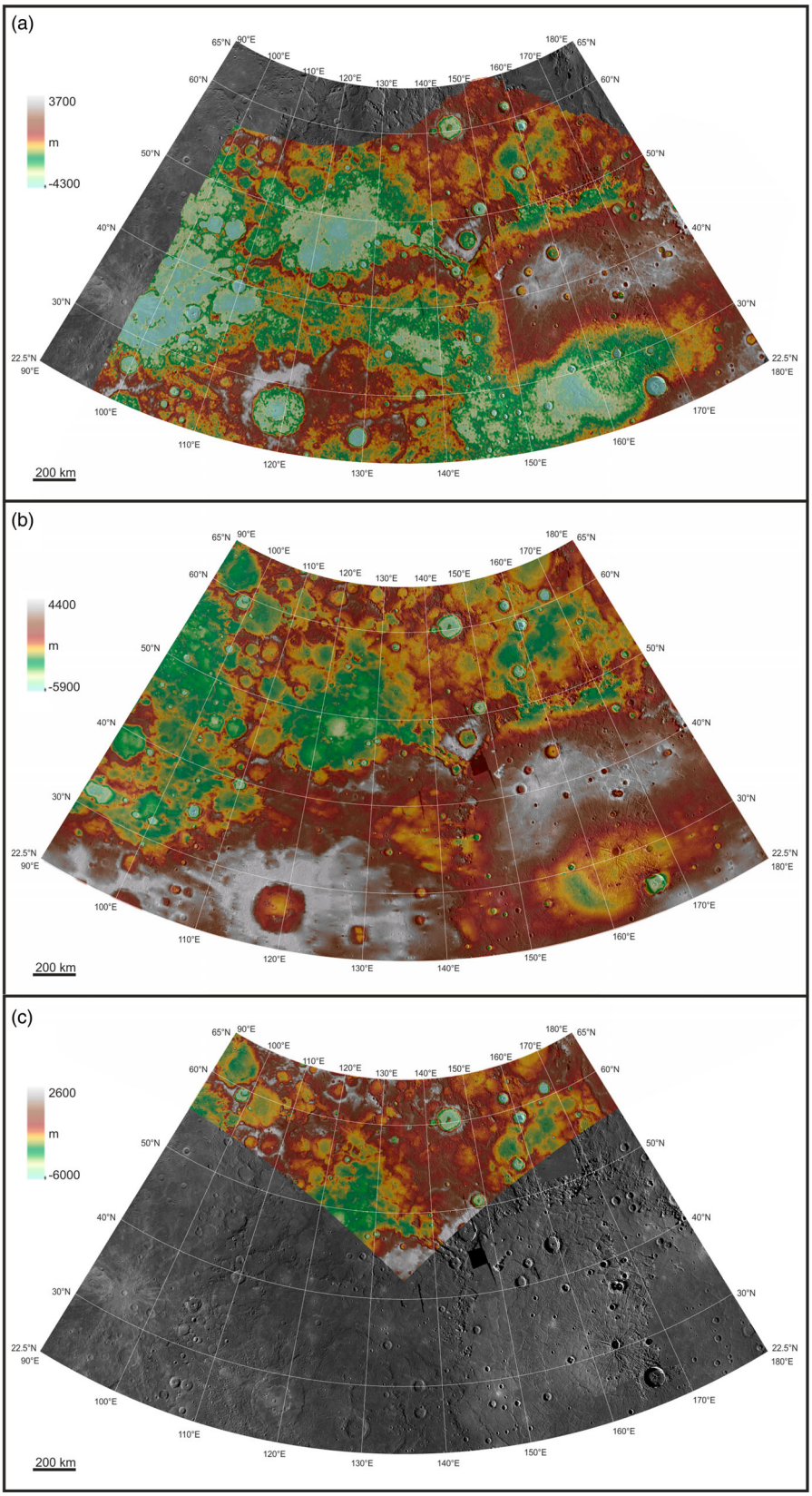

Figure 2. Topographic dataset. (a) M1 portion of the stereo-derived DTM (Mancinelli et al., 2015; Preusker et al., 2011) with a resolution of 1 km/pixel. Due to systematic noise in the original portion M1 of the DTM from Preusker et al. (2011), this was filtered with a 5×5 kernel low-pass filter (LPF) and fast Fourier (FFT), adding back 20% of the original value in order to preserve the spatial context (Mancinelli et al., 2015). (b) Portion of the northern hemisphere DTM at a resolution of 665 m/pixel (Zuber et al., 2012). (c) Portion of the northern polar DTM with a resolution of 500 m/pixel (Zuber et al., 2012). Despite that the northern hemisphere MLA DTM covers a larger portion of the quadrangle, it loses resolution at mid- and low latitudes (Figure 2(b)). Therefore, we used the M1 portion of the DTM (Preusker et al., 2011) as the main topographic support for the southern half of the map, the northern hemisphere DTM for the western boundary and the polar DTM for the northern part of the quadrangle. Scale values refer to the standard parallels.

Table 1. Examples of small features (<2 km) considered of interest for further investigation.

Feature type	Type location
Bright spots on crater walls	33.8°N, 120.7°E
Pyroclastic deposits	58.4°N, 161.2°E
Conic features	34.7–36.7°N, 138.5–141.5°E
Flow morphologies in Angkor Vallis	58.3°N, 113°E
Interesting tectonic structures	55.1°N, 177.6°E
Positive relief within a volcanic vent	48.7°N, 159.5°E

files covering the quadrangle. The original image (.img) data were converted to cube (.cub) files, then projected and finally mosaicked to obtain the imagery base map (Figure 1(a)) which was imported in to QGIS (see Software section) for mapping.

The geologic mapping of the units and of the geomorphic features was achieved through the following steps: (i) delineation of contact relationships to define unit boundaries (linear shapefiles); (ii) definition and coloring of the map units (polygon shapefiles from linear boundaries); and (iii) mapping of geomorphic features and structures (point and linear shapefiles). Mapping of features in the geographical information system (GIS) was at sufficient precision to be represented at the map scale and avoid the digitization of details that were too small (Tanaka, Skinner, & Hare, 2011). To produce the attached Main Map at a scale of 1:3,000,000, we mapped at an average scale of 1:450,000 (with a range of 1:300,000–1:600,000).

Contacts between units have been mapped as certain or approximate. We considered a contact certain if it allows the confident location of the boundary between features within the mapping scale range (Tanaka et al., 2011), while a contact is considered approximate if, at the mapping scale, it is located with poor or uncertain confidence (Tanaka et al., 2011). Faults have been mapped as certain or uncertain, with the uncertainty of the structure given by the interpretation of its kinematics and not by its location.

Symbologies for linear and point features were defined, when available, according to the digital cartographic standard for the geologic map symbolization of the planetary geologic features from the Federal Geographic Data Committee (see FGDC).

Crater rims were classified as small buried and small certain (diameter between 10 and 20 km) or large certain (diameter greater than 20 km). Crater centers were classified as large peak craters, small peak craters and craters (large and small) without a peak. Peak ring crests were mapped as linear features where observed. Volcanic vents (rimless and irregular depressions, endogenic pits) were mapped integrating previous catalogs (Denevi et al., 2013; Thomas, Rothery, Conway, & Anand, 2014b). Thrust faults have been mapped using the triangular symbol located on the hangingwall while the graben symbology indicates only the trace of the structure. Hollow clusters (Hc) smaller than 2 km (e.g. 49°N, 134°E; 48.5°N, 139.6°E) were mapped with point symbols. Features smaller than 2 km considered of interest for further investigation were mapped with points (see Table 1).

Craters, vallis and other features were named according to the Gazetteer of Planetary Nomenclature (http://planetarynames.wr.usgs.gov/) of the International Astronomical Union (IAU) as of December 2015.

Mapped terrains were divided into geologic units and crater materials. The geologic units are classified on the basis of their morphology, relative reflectance, spatial relationships and previous studies. In particular, the main units (i.e. IP, SP, Odin Formation, Bright Intercrater Plains (BIP) and Caloris Rough Ejecta (CRE)) were defined according to their definition in previous work (Blewett et al., 2011, 2012; De Hon, Scott, & Underwood, 1981; Denevi et al., 2009, 2013; Grolier & Boyce, 1984; Guest & Greeley, 1983; King & Scott, 1990; Mancinelli et al., 2015; McGill & King, 1983; Schaber & McCauley, 1980; Spudis & Prosser, 1984; Strom, Malin, & Leake, 1990; Trask & Dzurisin, 1984) and their morphologic type and geographic names (e.g. Caloris Smooth Plains, CSP). All the craters larger than 20 km found in the quadrangle were classified into three classes, from the most degraded C_1 to the fresh and well preserved C_3 (Figure 3). This classification was produced considering the superposition of later craters and the degree of preservation of the impact-derived morphologies such as rims, walls, peaks and ejecta blankets. Terrains constituting the infill of these craters were named according to their smooth (Sci) or hummocky (Hci) morphology. Deposits related to crater floor and ejecta of craters with diameter between 10 and 20 km have not been mapped and thus appear undivided from the target unit. Only the rim and center of these small craters are reported on the map as linear and punctual features, respectively. The smooth deposits locally found inside these small craters were included in the SP unit. Craters smaller than 10 km and fields of secondary craters are abundant across the entire map. However, these have not been mapped in order to avoid saturation of map features and so focus on unit boundaries (e.g. ~50–65°N, 110–140°E) and tectonic features (e.g. Caloris basin). Ejecta chains were mapped only outside of the ejecta blanket of the parent crater and only where the clear evidence of chained craters was detectable at the mapping scale. A classification was attempted for each ejecta chain based on the interpreted parent crater of the chain. Each chain is classified by the subscript of its label which reflects the class of the interpreted parent crater class (Ej_1 has a class 1 parent crater, Ej_3 has a class 3 parent crater), for the chains where the parent crater was undefined the label is Ej_u. Parameters used for this classification are the presence of a large primary impact and the radial distribution of crater chains with respect to this major impact (e.g. region

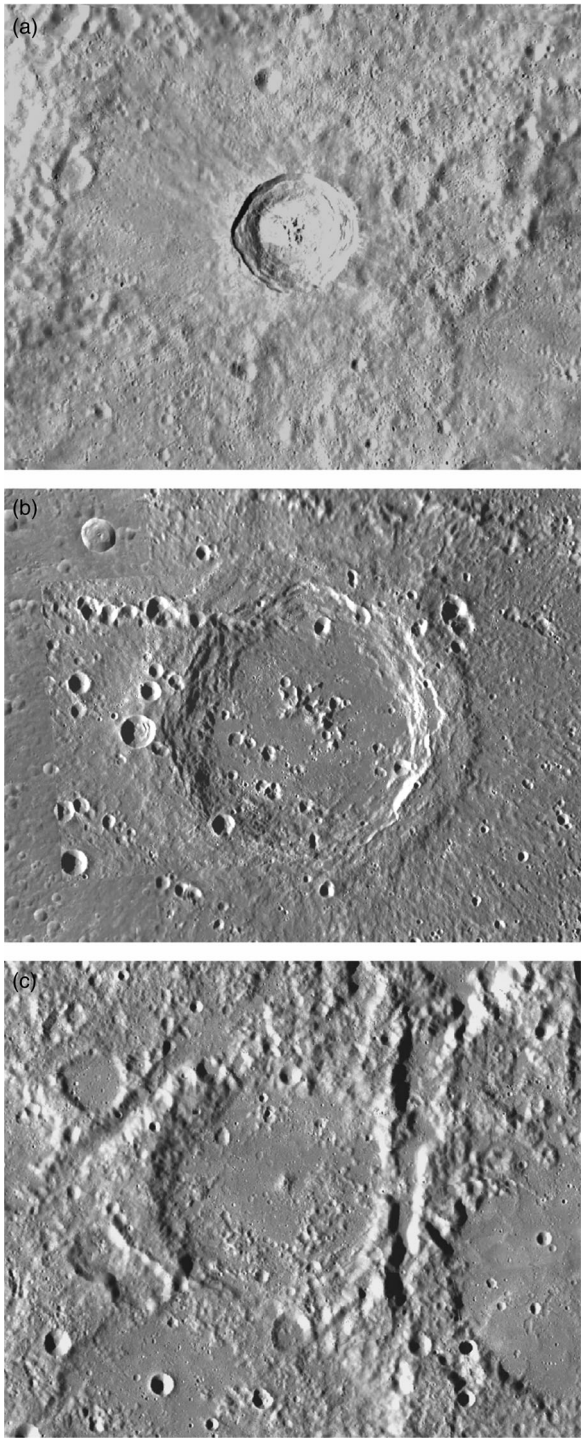

Figure 3. Sample craters representing the three classes used to classify all the craters larger than 20 km in this work. These classes are defined on the basis of degradation of the crater materials (walls, peak and rim) and superposition of mantling units and/or fresher primary or secondary craters (e.g. Galluzzi, 2015). (a) C_3 – Fonteyn crater (32.8°N, 95.6°E) which is ~29 km in diameter. Note that the continuity and sharpness of the rim and crater walls are well defined and superposed craters are absent. (b) C_2 – Kerouac crater (25.2°N, 129.4°E) which is ~110 km in diameter. Note the abundance of superposed craters, the floor is partially filled, rim is continuous and ejecta are preserved. (c) C_1 class – unnamed crater (54.8°N, 104°E) which is ~63 km in diameter. Note that the rim is discontinuous and walls and ejecta are severely degraded.

surrounding Raditladi crater: ~22.5–40°N to 110–130° E).

To constrain the epoch of formation of the main units found in the area, we exploited the catalog of craters larger than 10 km resulting from this work, to produce a Cumulative Size-Frequency Distribution (CSFD) for sample areas,[2] using the Craterstats2 software (see Software section).

4. Description of map units

The terrains mapped throughout the H04 quadrangle are divided into Geologic Units and Crater Materials. We present a brief interpretation of the plausible formation of the materials constituting the geologic units along with the description of each unit. The interpretation is given considering both the morphologies observed in the area and, where available, the interpretations given to the unit by previous work. Example localities representing the morphological features of the geologic units and the spatial relations between the units are shown in Figure 4.

Crater materials are described according to their class and morphology and have not been interpreted because each impact, representing an event with peculiar morphologies and products, requires local detailed investigation (e.g. Mancinelli et al., 2015). Each polygonal deposit is labeled according to the code of its unit.

5. Geologic units

Hollow clusters: Shallow depressions with flat floors surrounded by bright deposits and mainly found on floors, peaks or walls of impact craters. These sub-kilometer depressions are often grouped in clusters and are related to craters that targeted low-reflectance materials (e.g. unnamed craters at 23–25.5°N, 179.5° E; Kertész crater 27.5°N, 146.5°E). The Hc deposits catalog produced in previous work (Blewett et al., 2011, 2012; Thomas, Rothery, Conway, & Anand, 2014a) was included and integrated in the present map. *Interpretation*: sublimation or degassing-induced collapse of low-reflectance materials shocked by impact, volcanic or thermal events (Blewett et al., 2011, 2012; Thomas et al., 2014a; Xiao et al., 2013).

Caloris Smooth Plains: Smooth material occurring inside the Caloris basin (e.g. 33°N, 172°E). These deposits have entirely filled the basin produced by the Caloris impact. Spectral evidence (Weider et al., 2015) suggests that these materials are different in composition if compared to Caloris-surrounding and Northern SP. The extent of CSP is interpretative because the transition between SP and CSP is unclear.

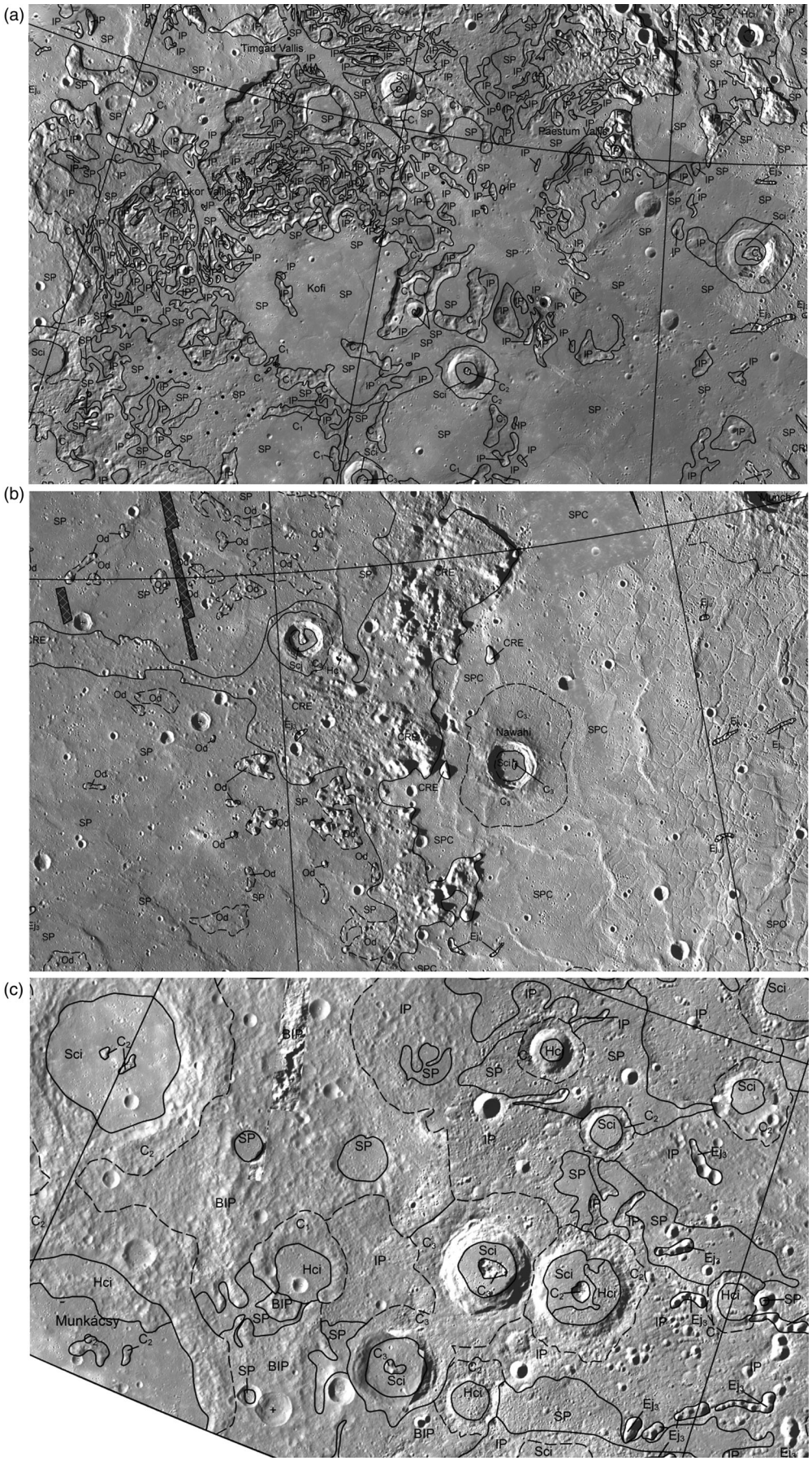

Figure 4. Sample localities representing the morphological characteristics and spatial relationships between the main geological units. Black solid and dashed lines represent certain and approximate contacts between units, respectively. (a) SP embaying IP, the image is centered at ~58°N, 120°E. (b) SP embaying Od and CRE with CSP inside the Caloris basin, the image is centered at 36°N, 143°E. (c) BIP and IP contacts, the image is centered at 26°N, 105°E.

Radial and circumferential grabens and wrinkle ridges are observed on these deposits. Most of the tectonic structures observed inside the Caloris basin are radially distributed around the Apollodorus impact crater (~30.5°N, 163°E). However, it is unlikely that this relatively small impact event could have produced such deformation which is rather attributed to later stages of deformation of the CSP (Watters et al., 2009). Interestingly, these two distinct sets of structures (radial and circumferential grabens inside Caloris) do not intersect with each other, possibly indicating two distinct phases or regimes of deformation of the CSP. *Interpretation*: volcanic deposits (Weider et al., 2015) produced in the Caloris impact basin and subsequently deformed by grabens and wrinkle ridges and targeted by later impact events (Watters et al., 2009).

Smooth Plains: Smooth material widely occurring across the quadrangle. These deposits fill impact basins and depressions producing patterns and morphologies typical of flow events (e.g. Angkor Vallis, 57°N, 115°E) (Byrne et al., 2013; Denevi et al., 2013). These are found in the annular deposits surrounding Caloris and in the western part of the map, filling impact basins and partially covering the basal geologic and crater units (e.g. Paestum Vallis, 61°N, 127°E; Caral Vallis, 63°N, 129°E). On these deposits, wrinkle ridges are locally found. The smallest SP deposits are found on the floor of craters with a diameter between 10 and 20 km; these deposits are mainly located in the western half of the quadrangle. SP are generally darker and less deformed than CSP (Figure 4(b)). Ostrach et al. (2015) estimated the thickness of the northern SP to range between ~0.7 and ~1.8 km. Locally (e.g. 59°N, 109.5°E; 58°N, 101°E) SP are found in conjunction with volcanic vents. SP deposits were targeted mainly by C_3 craters. *Interpretation*: volcanic deposits (Byrne et al., 2013; Denevi et al., 2013; Weider et al., 2015) locally produced and linked to impact events (e.g. unnamed crater at 59°N, 110°E).

Odin formation: Patches and large deposits of smooth materials encompassing blocks, surrounding the Caloris basin that are found up to distances of 700 km from the basin (e.g. 52.5°N, 123°E). When in contact with SP, the boundaries of these deposits with SP are less confidently located due to SP embayment (e.g. the region east of Solitudo Phoenicis ~23–26°N, 134–141°E). In these cases, their boundary is defined by the extent of the blocks. Conic features are locally observed on Od deposits (e.g. ~34.6–36.6°N, 138.4–141.5°E). *Interpretation*: Caloris-related ejecta material that was not entirely covered by subsequent smooth deposits (Denevi et al., 2013; Fassett et al., 2009; Guest & Greeley, 1983; Mancinelli et al., 2015; McCauley, Guest, Schaber, Trask, & Greeley, 1981).

Caloris Rough Ejecta: Hummocky and undulating materials surrounding the Caloris impact basin. Unlike the Od deposits, CRE show clear boundaries both internally with CSP and with SP in the external circum-Caloris annulus (Mancinelli et al., 2015) (e.g. ~40–50°N, 140–150°E). Small patches of CRE are found up to 500–600 km from the basin rim and are attributed to CRE because of their undulating morphology and their radial distribution with respect to Caloris. CRE deposits were targeted by C_2–C_3 craters and in the central area of the map (44°N, 132°E) are in contact with C_1 crater materials. This unit encompasses terrain previously mapped as Van Eyck, Montes and Nervo formations (Fassett et al., 2009; Guest & Greeley, 1983; Mancinelli et al., 2015). *Interpretation*: materials shocked, melted, mixed and ejected by the Caloris impact and thus coeval with it (Fassett et al., 2009; Mancinelli et al., 2015).

Bright Intercrater Plains: Hummocky and heavily cratered terrain with clear boundaries with SP (e.g. 62°N, 137°E). In general, these materials are topographically higher than surrounding deposits and are in lateral continuity with IP. BIP materials show the higher reflectance across the entire map. BIP deposits were targeted by C_1–C_3 craters. *Interpretation*: old deposits with a morphological and topographic signature very similar to IP but with higher reflectance (Mancinelli et al., 2015).

Intercrater Plains: Hummocky, heavily cratered terrains with clear boundaries with SP. These terrains are topographically higher than surrounding deposits and are partially covered by SP. IP are mainly found in the western half of the map, where they are not buried by SP deposits (e.g. region between Angkor, Paestum and Timgad vallis ~56–63°N, 110–130°E). These materials show relatively lower reflectance than BIP. IP deposits were targeted by C_1–C_3 craters. *Interpretation*: old terrains with possible volcanic origin (e.g. Malin, 1976; Mancinelli et al., 2015; Spudis & Guest, 1988; Strom, 1977) and surface expression different from BIP. IP represent the main basal unit on which SP terrains were deposited.

6. Crater materials

Ejecta crater chains: Secondary crater chains in a radial distribution with respect to the primary impact craters. Where possible, the parent crater of each chain is interpreted and the chain is classified according to the class of the parent crater (Ej_1–Ej_3), in all other cases it is classified as uncertain (Ej_u).

Hummocky Crater infill: Hummocky and undulating material found on the floor of craters larger than 20 km.

Smooth Crater infill: Smooth material found on the floor of craters larger than 20 km.

Crater class C_3: Material of impact craters with a diameter larger than 20 km with sharp rim and peak, clear wall terraces and extended ejecta blankets. Rays and bright materials are observed in the ejecta of the

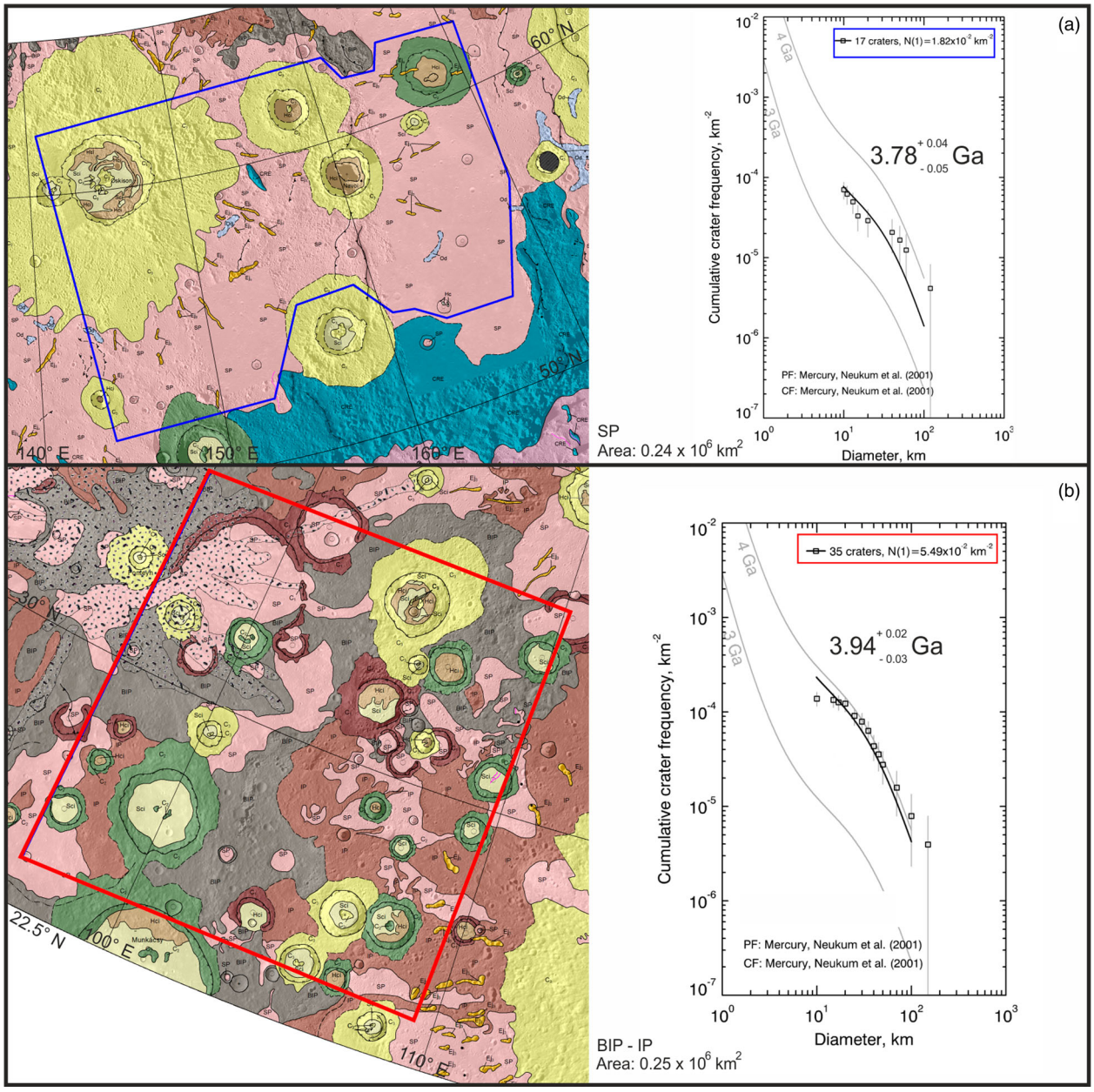

Figure 5. Blue and red squares indicate sample areas for SP (a) and for terrains with IP and BIP (b) where absolute ages were estimated. Area values refer to the extent of the squares. The chronology and production function used to fit the observed CSFD are from Neukum, Ivanov, et al. (2001). The small patches of Od and CRE in the blue square of (a) have not been included in the area used for the age estimates. The area used for BIP – IP age estimate in the red square in (b) includes all the SP events that partially embayed or covered IP and BIP which are assumed to be the basal units on which these SP were deposited. To estimate IP and BIP age, only craters fully superposed to SP were not included in the CSFD (G. G. Michael, personal communication). See the text and attached Main Map for unit descriptions.

fresher craters. These craters are generally well preserved and, if compared to the fresher C_2, show less superposed craters. Deposits infilling C_3 craters are Hci and Sci. This class includes the youngest craters observed in the whole quadrangle. Type craters: Fonteyn (32.8°N, 95.6°E), Cunningham (30.3°N, 157.1°E) and unnamed crater (39.5°N, 110°E).

Crater class C_2: Material of impact craters with a diameter larger than 20 km with no rays and absent, degraded or buried peak. Their rims are continuous but less sharp than C_3 craters. Walls are terraced only around larger craters. Ejecta blankets have moderate-to-poor extension and are best preserved in larger craters. These craters have a moderate-to-high density of superposed younger craters. Deposits infilling C_2 crater floors are mainly Sci and Hci. Type craters: Poe (43.7°N, 159.1°E) and Kerouac (25.2°N, 129.4°E).

Crater class C_1: Material of impact craters with a diameter larger than 20 km with no rays, and highly modified and discontinuous rims. Their walls, where not buried, are poorly preserved. Ejecta blankets are poor-to-absent. Deposits infilling C_1 crater floors are mainly SP. C_1 features represent the oldest detectable crater materials in the whole quadrangle and often are in clear lateral contact with IP or BIP units. Type craters: unnamed crater (54.8°N, 104°E) and unnamed crater (60°N, 117°E).

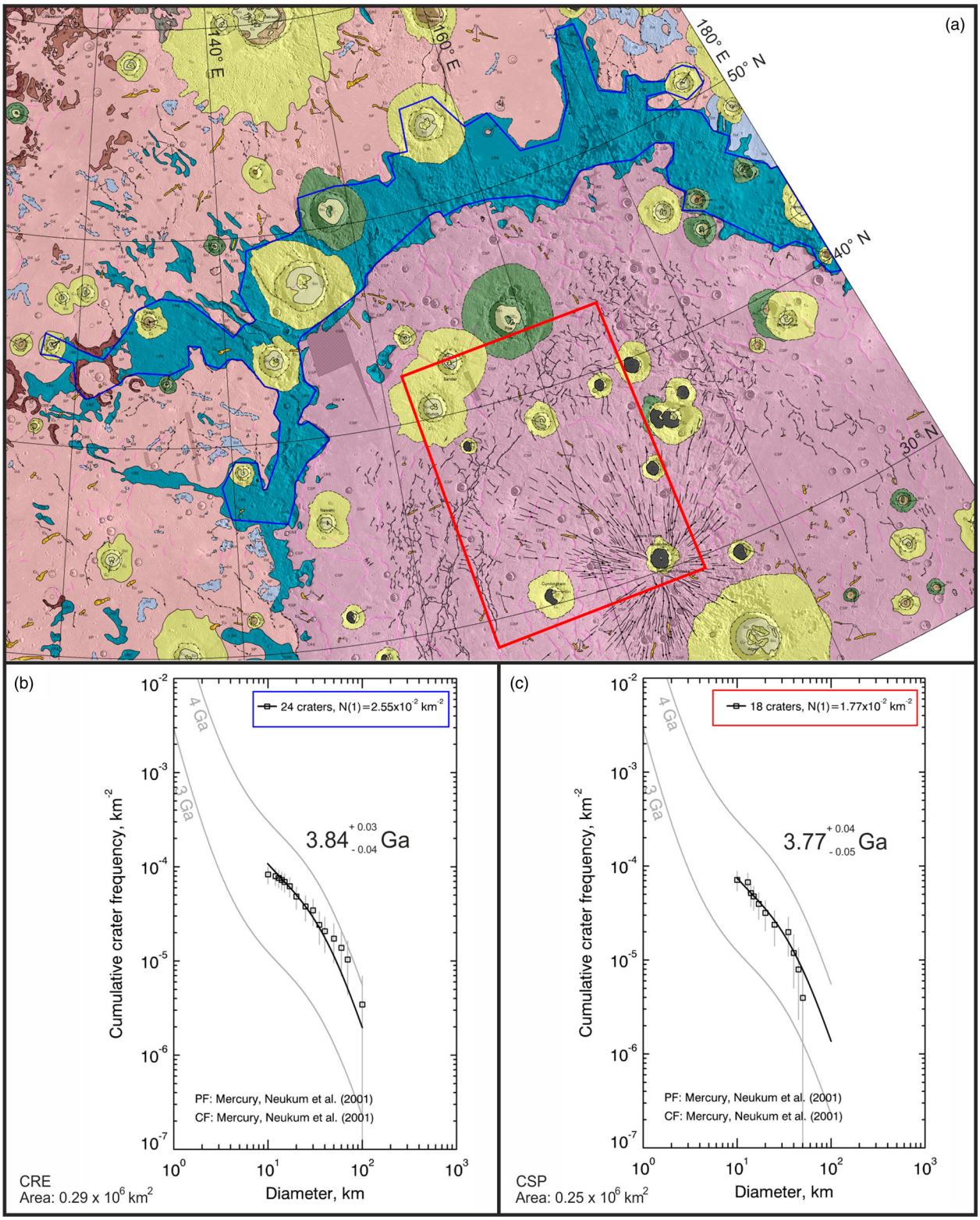

Figure 6. (a) Blue polygon and red square indicate sample areas where the absolute ages were estimated for CRE (b) and CSP (c). The chronology and production function used to fit the observed CSFD are from Neukum, Ivanov, et al. (2001). The area used for CRE age estimate includes the SP mantling events which partially embayed or covered the crater basins that targeted CRE. See the text and attached Main Map for unit descriptions.

7. Age estimates

Once the mapping was completed, we defined some sample areas where the CSFDs of the main geologic units were calculated using the catalog of craters larger than 10 km compiled during the mapping. To estimate absolute ages of the units, we fit the observed CSFD of the sample area (see Section 3)[2] with an impactor flux CSFD (Neukum, Ivanov, & Hartmann, 2001). The sample areas were chosen in order to constrain lower (older) and upper (younger) temporal limits for the mapped area considering the crater density and superposition order of the geologic units. Four sample areas

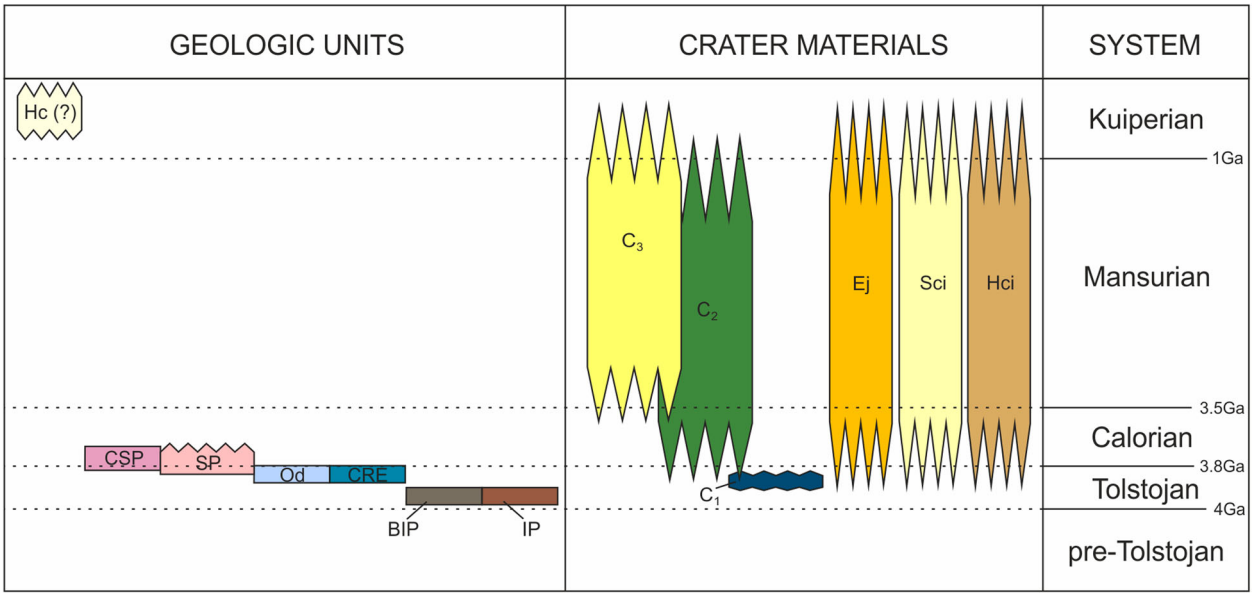

Figure 7. Correlation of map units as inferred from superposition, surface degradation and absolute age estimates of the sample regions representative of the geologic units. CRE time range is representative also of the Caloris impact event. The geologic time scale is from Neukum, Oberst, Hoffmann, Wagner, and Ivanov (2001). The reader, however, should consider these absolute ages as indicative and likely inadequate for a local investigation, particularly for the crater units, whose dating is relative and based on morphology and superposition order.

with comparable area extent were defined in order to produce age estimates for the IP-BIP, SP, CRE and CSP units. The area representative for IP-BIP units is located in the south-western portion of the quadrangle (centered at ~30°N, 105°E) while the area for the SP unit is found north of Caloris, centered at ~57°N, 155° E (Figure 5). CRE age was estimated from the larger CRE deposit north of the Caloris basin while the CSP sample area is located inside the Caloris basin (centered at ~35°N, 159°E).

Results show that the SP found north of Caloris (Figure 5(a)) have an average estimated age of 3.78 ± 0.045 Ga. Whereas in the area where IP and BIP terrains are abundant, the estimated age is 3.94 ± 0.025 Ga (Figure 5(b)).

In order to chronologically locate the Caloris impact in the geologic context, we produced CSFDs and age estimates for areas representative of the CRE and CSP units (Figure 6). Results show that, with slight error superposition, the terrains mapped as CRE, with an estimated age of 3.84 ± 0.035 Ga, are likely older than CSP (3.77 ± 0.045 Ga) and surrounding SP (3.78 ± 0.045 Ga) (Figures 5(a), 6(b) and 6(c)). Considering that CRE encompasses materials that are likely coeval with the Caloris impact event (Fassett et al., 2009; Mancinelli et al., 2015; this work), by estimating the age of formation of the CRE unit, a temporal constraint is provided for the Caloris impact event (i.e. 3.84 ± 0.035 Ga).

8. Correlation of map units

The mapping process allowed a detailed investigation of the relative stratigraphic order of the main units found in the quadrangle (Figure 7). The uncertainties determined from the crater CSFDs were used as upper and lower bounds for the main geologic units in the map area. Jagged upper or lower edges indicate uncertainties in the temporal extent of a unit.

An upper (younger) absolute age constraint for SP shown in Figure 7 is undefined because we cannot exclude that some deposits of SP in the northern and north-western portions of the quadrangle are younger than 3.74 Ga. However, in this case, the minimum age limit is set to 3.69 Ga by Ostrach et al. (2015), if the same production function as used in this work (i.e. Neukum, Ivanov, et al., 2001) is considered. The size of the hollow clusters found in the mapped area (e.g. 26°N, 179.8°E; Kertész crater 27.3°N, 146.2°E) represents the major limit for the definition of the age of these features using crater counting. Thus, for the purpose of this work, the Hc timing is approximated both considering upper and lower limits and its total temporal extent. However, based on the observation that hollows appear to form long after the host impact crater (Blewett et al., 2011), we consider Hc as the youngest geologic unit observed in the whole area.

Deposits mapped as Od and CRE are considered to be coeval and representative of the Caloris impact event (Denevi et al., 2013; Fassett et al., 2009; Guest & Greeley, 1983; Mancinelli et al., 2015; McCauley et al., 1981) and, considering average age estimates, these are older than CSP deposits filling the Caloris basin, with slight temporal superposition if the estimates' errors are considered.

Older terrains are found within IP and BIP units, consistently with the interpretations given in this and

in previous work (e.g. Mancinelli et al., 2015; Strom, 1977). However, considering the morphological and spatial distribution of the IP and BIP units (map in Figure 5(b)), the age estimate produced in this work is hardly attributable solely to IP or to BIP terrains and thus, for the purpose of this work, we consider this value as being representative of both units and in general of the oldest terrains mapped in the area.

Crater materials have less defined temporal constraints due to uncertainties in the epoch of formation of each event and of each class relatively to older and younger classes. The only relative constraint is given by superposition of younger craters to older (this also contributes to class definition for each crater) and by the observation that C_1 craters are locally superposed to BIP and IP materials in the western portion of the quadrangle.

9. Conclusions

The geologic map of the Raditladi quadrangle (H04) of Mercury presented in this work was produced to constrain the geological and morphological analysis of this intriguing and important region of Mercury. The observed geologic scenario is the result of contributions by impact cratering and volcanic events. The current geologic framework of the area was achieved within a period of ~0.24 Ga, between 3.96 and 3.72 Ga. After the emplacement of the BIP and IP terrains, the Caloris impact produced the Caloris basin and surrounding CRE terrains, marking a significant change to the geology of the region. The subsequent volcanic phase led to the emplacement of CSP and its later tectonic deformation that was likely driven by cooling. Emplacement of the SP, that partially mantled the older units (e.g. 52–62°N, 110–130°E), likely represents the latest region-wide geologic phase. Since ~3.72 Ga, only local-scale phenomena such as impact cratering and hollow formation has affected the area. However, more work is required to answer questions arising from these local-scale features. With this map, the reader is provided with a useful tool to produce a higher scale mapping and advanced investigations to address these questions. Furthermore, this map, along with other similar products, could also support the targeting of the instruments onboard the forthcoming BepiColombo ESA/JAXA joint mission by serving as a catalog of regions of interest.

Software

RDRBDR images were processed using the USGS Integrated Software for Imagers and Spectrometers (see ISIS3) (Eliason, 1997; Gaddis et al., 1997; Torson & Becker, 1997). GIS software: QuantumGIS 2.8.1 (QGIS – http://www.qgis.org). Fit of the craters' CSFD was produced using the Craterstats2 tool (e.g. Michael & Neukum, 2010; Platz, Michael, Tanaka, Skinner, & Fortezzo, 2013). The Craterstats2 software, together with complete references to the procedures it implements to fit data and estimate errors, can be found at http://www.geo.fu-berlin.de/en/geol/fachrichtungen/planet/software/index.html.

Notes

1. Hitherto, hollows represent a peculiar feature observed only on Mercury so far. They are often grouped in clusters, and their formation is still debated (Blewett et al., 2011, 2012; Thomas et al., 2014a; Xiao et al., 2013). These features are often found on walls or peak material of impact craters (e.g. Mancinelli et al., 2015; Thomas et al., 2014a) and always involve low-reflectance materials (Mancinelli et al., 2015; Thomas et al., 2014a; Xiao et al., 2013). Volcanic contribution to the geologic scenario found in the H04 quadrangle is significant. In fact, based on morphological and compositional evidence, the majority of the Smooth Plains found in the quadrangle are volcanic in origin, including deposits found in the northern portion of the quadrangle (Head et al., 2011; Byrne et al., 2013; Denevi et al., 2013; Ostrach et al., 2015; Weider et al., 2015) and filling the Caloris basin (Watters et al., 2009; Weider et al., 2015). Moreover, the Smooth Plains found inside Caloris show distinctive composition with respect to the northern volcanic deposits (Weider et al., 2015).
2. The number of craters found in a definite region is generally used to relatively date this region with respect to others of the same target body, through the principle that the higher the number of craters, the older is the surface on which these craters were counted. Once the CSFDs of these areas is known, by appropriate scaling and comparison with lunar data, the absolute ages of the sample areas can be estimated assuming a production function for the impactor flux (Crater Analysis Techniques Working Group, 1978; Hartmann et al., 1981; Neukum & Ivanov, 1994; Neukum, Ivanov, et al., 2001). In the age estimates included, all the craters (irrespective of their class) larger than 10 km that targeted the unit/units of interest together with the area covered by the crater material and by eventual embaying and covering superposed material. Only craters entirely superposed on younger or older units were excluded from the estimates together with the area they cover – for example, some small craters that targeted SP in Figure 5(b) (G. G. Michael, personal communication).

Acknowledgments

We acknowledge the insightful edits of Jennifer E. Carrell, David A. Crown and Valentina Galluzzi; we also acknowledge the editorial handling by Monica Pondrelli. This work has made use of the USGS Integrated Software for Imagers and Spectrometers (ISIS3), we thank the developers and creators of the software. We also thank the creators and developers of the QGIS software. We thank the MESSENGER team for making available the data used in this work.

Disclosure statement

No potential conflict of interest was reported by the authors.

ORCID

Paolo Mancinelli http://orcid.org/0000-0003-4524-3199

References

Blewett, D. T., Chabot, N. L., Denevi, B. W., Ernst, C. M., Head, J. W., Izenberg, N. R., … Hurwitz, D. M. (2011). Hollows on Mercury: MESSENGER evidence for geologically recent volatile-related activity. *Science*, *333*, 1856–1859.

Blewett, D. T., Vaughan, W. M., Xiao, Z., Chabot, N. L., Denevi, B. W., Ernst, C. M., … Solomon, S. C. (2012). Mercury's hollows: Constraints on formation and composition from analysis of geological setting and spectral reflectance. *Journal of Geophysical Research: Planets*, *118*, 1013–1032. doi:10.1029/2012JE004174

Byrne, P. K., Klimczak, C., Williams, D. A., Hurwitz, D. M., Solomon, S. C., Head, J. W., … Oberst, J. (2013). An assemblage of lava flow features on Mercury. *Journal of Geophysical Research: Planets*, *118*, 1303–1322. doi:10.1002/jgre.20052

Byrne, P. K., Watters, T. R., Murchie, S. L., Klimczak, C., Solomon, S. C., Prockter, L. M., & Freed, A. M. (2012). *A tectonic survey of the Caloris basin, Mercury*. 43rd Lunar and Planetary Science Conference, 1722, The Woodlands, Texas.

Crater Analysis Techniques Working Group. (1978). *Standard techniques for presentation and analysis of crater size-frequency data*. NASA Technical memorandum of the Science and Technical Information Office 79730.

De Hon, R. A., Scott, D. H. and Underwood, J. R. Jr. (1981). *Geologic map of the Kuiper (H-6) quadrangle of Mercury*. United States Geological Survey, Geologic Investigations Series, Map I-1233.

Denevi, B. W., Ernst, C. M., Meyer, H. M., Robinson, M. S., Murchie, S. L., Whitten, J. L., … Peplowski, P. N. (2013). The distribution and origin of smooth plains on Mercury. *Journal of Geophysical Research: Planets*, *118*, 891–907. doi:10.1002/jgre.20075

Denevi, B. W., Robinson, M. S., Solomon, S. C., Murchie, S. L., Blewett, D. T., Domingue, D. L., … Chabot, N. L. (2009). The evolution of Mercury's crust: A global perspective from MESSENGER. *Science*, *324*, 613.

Eliason, E. M. (1997). *Production of digital image models using the ISIS system*. Lunar Planet. Sci. XXVIII, Houston, Texas, Abstract #1198.

Fassett, C. I., Head, J. W., Blewett, D. T., Chapman, C. R., Dickson, J. L., Murchie, S. L., … Watters, T. R. (2009). Caloris impact basin: Exterior geomorphology, stratigraphy, morphometry, radial sculpture, and smooth plains deposits. *Earth and Planetary Science Letters*, *285*, 297–308.

FGDC (Federal Geographic Data Committee). *Digital cartographic standard for geologic map symbolization*. Document number FGDC-STD-013-2006, Planetary Geologic Features. Retrieved from http://ngmdb.usgs.gov/fgdc_gds/geolsymstd.php

Frigeri, A., Federico, C., Pauselli, C., & Coradini, A. (2009). *Fostering digital geologic maps: the digital geologic map of Mercury from the USGS Atlas of Mercury, Geologic Series*. 40th Lunar and Planetary Science Conference, March 23–27, 2009, The Woodlands, Texas. Lunar and Planetary Institute, Houston, TX, abstract 2417.

Gaddis, L., Anderson, J., Becker, K., Becker, T., Cook, D., Edwards, K., … Torson, J. (1997). *An overview of the integrated software for imaging spectrometers*. Lunar Planet. Sci. XXVIII, Houston, Texas, Abstract #1226.

Galluzzi, V. (2015). *Structural analysis of the Victoria quadrangle (H2) of Mercury based on NASA MESSENGER data*. Ph.D. thesis, Università degli Studi di Napoli "Federico II".

Grolier, M. J., & Boyce, J. M. (1984). *Geologic map of the Borealis Region (H-1) of Mercury*. United States Geological Survey, Miscellaneous Investigations Series, Map I-1660.

Guest, J. E., & Greeley, R. (1983). *Geologic map of the Shakespeare (H-3) quadrangle of Mercury*. United States Geological Survey, Miscellaneous Investigations Series, Map I-1408.

Hartmann, W. K., Strom, R. G., Grieve, R. A. F., Weidenschilling, S. J., Diaz, J., Blasius, K. R., … Jones, K. L. (1981). *Chronology of planetary volcanism by comparative studies of planetary craters. Basaltic volcanism on the terrestrial planets*. Elmsford, NY: Pergamon Press.

ISIS3. *USGS Integrated Software for Imagers and Spectrometers (ISIS)*, the software and its manual are Retrieved from https://isis.astrogeology.usgs.gov/

King, J. S., & Scott, D. H. (1990). *Geologic map of the Beethoven (H-7) quadrangle of Mercury*. United States Geological Survey, Miscellaneous Investigations Series, Map I-2048.

Malin, M. C. (1976). Observations of intercrater plains on Mercury. *Geophysical Research Letters*, *3*, 581–584.

Mancinelli, P., Minelli, F., Mondini, A., Pauselli, C., Federico, C. (2015). A downscaling approach for geological characterization of the Raditladi Basin of Mercury. In T. Platz, M. Massironi, P. K. Byrne, and H. Hiesinger (Eds.), *Volcanism and tectonism across the inner solar system. geological society* (pp. 57–75). London: Special Publications (401, First published online March 11, 2014).

McCauley, J. F., Guest, J. E., Schaber, G. G., Trask, N. J., & Greeley, R. (1981). Stratigraphy of the Caloris basin, Mercury. *Icarus*, *47*, 184–202.

McGill, G. E., & King, E. A. (1983). *Geologic map of the Victoria (H-2) quadrangle of Mercury*. United States Geological Survey, Miscellaneous Investigations Series, Map I-1409.

Michael, G. G., & Neukum, G. (2010). Planetary surface dating from crater size–frequency distribution measurements: Partial resurfacing events and statistical age uncertainty. *Earth and Planetary Science Letters*, *294*, 223–229. doi:10.1016/j.epsl.2009.12.041

Neukum, G., & Ivanov, B. A. (1994). Crater size distributions and impact probabilities on Earth from lunar, terrestrial-planet, and asteroid cratering data. In T. Gehrels (Eds.), *Hazard Due to comets and asteroids* (pp. 359–416). Tucson, AZ, USA: The University of Arizona Press.

Neukum, G., Ivanov, B. A., & Hartmann, W. K. (2001). Cratering records in the inner solar system in relation to the lunar reference system. *Space Sience Review*, *96*, 55–86.

Neukum, G., Oberst, J., Hoffmann, H., Wagner, R., & Ivanov, B. A. (2001). Geologic evolution and cratering history of Mercury. *Planetary and Space Science*, *49*, 1507–1521.

Ostrach, L. R., Robinson, M. S., Whitten, J. L., Fassett, C. I., Strom, R. G., Head, J. W., & Solomon, S. C. (2015). Extent, age, and resurfacing history of the northern smooth plains

on Mercury from MESSENGER observations. *Icarus*, *250*, 602–622.

Platz, T., Michael, G., Tanaka, K., Skinner, J. A., & Fortezzo, C. M. (2013). Crater-based dating of geological units on Mars: Methods and application for the new global geological map. *Icarus*, *225*, 806–827. doi:10.1016/j.icarus.2013.04.021

Preusker, F., Oberst, J., Head, J. W., Watters, T. R., Robinson, M. S., Zuber, M. T., & Solomon, S. C. (2011). Stereo topographic models of Mercury after three MESSENGER flybys. *Planetary and Space Science*, *59*, 1910–1917.

Schaber, G. G., & McCauley, J. F. (1980). *Geologic map of the Tolstoj (H-8) quadrangle of Mercury*. United States Geological Survey, Miscellaneous Investigations Series, Map I-1199.

Spudis, P. D., & Guest, J. E. (1988). Stratigraphy and geologic history of Mercury. In F. Vilas, C. R. Chapman, M. S. Matthews (Eds.), *Mercury* (pp. 118–164). Tucson: University of Arizona Press.

Spudis, P. D., & Prosser, J. G. (1984). *Geologic map of the Michelangelo (H-12) quadrangle of Mercury*. United States Geological Survey, Miscellaneous Investigations Series, Map I-1659.

Strom, R. G. (1977). Origin and relative age of lunar and mercurian intercrater plains. *Physics of the Earth and Planetary Interiors*, *15*, 156–172.

Strom, R. G., Malin, M. C., & Leake, M. A. (1990). *Geologic map of the Bach (H-15) quadrangle of Mercury*. United States Geological Survey, Miscellaneous Investigations Series, Map I-2015.

Tanaka, K. L., Skinner, J. A.Jr., and Hare, T. M. (2011). *Planetary geologic mapping handbook*. USGS Astrogeology Science Center. Retrieved from http://astrogeology.usgs.gov/search/details/Docs/Mappers/PGM_Handbook_2011/pdf

Thomas, R. J., Rothery, D. A., Conway, S. J., & Anand, M. (2014a). Hollows on Mercury: Materials and mechanisms involved in their formation. *Icarus*, *229*, 221–235.

Thomas, R. J., Rothery, D. A., Conway, S. J., & Anand, M. (2014b). Mechanisms of explosive volcanism on Mercury: Implications from its global distribution and morphology. *Journal of Geophysical Research*, *119*, 2239–2254. doi:10.1002/2014JE004692

Torson, J. M., & Becker, K. J. (1997). *ISIS – a software architecture for processing planetary images*. Lunar Planet. Sci. XXVIII, Houston, Texas, Abstract #1219.

Trask, N. J., & Dzurisin, D. (1984). *Geologic map of the discovery (H-11) quadrangle of Mercury*. United States Geological Survey, Miscellaneous Investigations Series, Map I-1658.

Watters, T. R., Murchie, S. L., Robinson, M. S., Solomon, S. C., Denevi, B. W., André, S. L., & Head, J. W. (2009). Emplacement and tectonic deformation of smooth plains in the Caloris basin, Mercury. *Earth and Planetary Science Letters*, *285*, 309–319.

Weider, S. Z., Nittler, L. R., Starr, R. D., Crapster-Pregont, E. J., Peplowski, P. N., Denevi, B. W., … Solomon, S. C. (2015). Evidence for geochemical terranes on Mercury: Global mapping of major elements with MESSENGER's X-ray spectrometer. *Earth and Planetary Science Letters*, *416*, 109–120.

Xiao, Z., Strom, R. G., Blewett, D. T., Byrne, P. K., Solomon, S. C., Murchie, S. L., … Helbert, J. (2013). Dark spots on Mercury: A distinctive low-reflectance material and its relation to hollows. *Journal of Geophysical Research – Planets*, *118*, 1752–1765. doi:10.1002/jgre.20115

Zuber, M. T., Smith, D. E., Phillips, R. J., Solomon, S. C., Neumann, G. A., Hauck, S. A. II, & Peale, S. J. (2012). Topography of the northern hemisphere of Mercury from MESSENGER laser altimetry. *Science*, *336*, 217–220.